Icarus 365 (2021) 114492

Contents lists available at ScienceDirect

Icarus

journal homepage: www.elsevier.com/locate/icarus

Creation of Lunar and Hermean analogue mineral powder samples for solar wind irradiation experiments and mid-infrared spectra analysis

Noah Jäggi [a,*], André Galli [a], Peter Wurz [a], Herbert Biber [b], Paul Stefan Szabo [b], Johannes Brötzner [b], Friedrich Aumayr [b], Peter Michael Edward Tollan [c], Klaus Mezger [c]

[a] *Physikalisches Institut, Universität Bern, Sidlerstrasse 5, CH-3012 Bern, Switzerland*
[b] *Institut für Angewandte Physik, TU Wien, Wiedner Hauptstraße 8-10/E134, A-1040 Vienna, Austria*
[c] *Institut für Geologie, Universität Bern, Baltzerstrasse 1 + 3, CH-3012 Bern, Switzerland*

ARTICLE INFO

Keywords:
Moon, surface
Mercury, surface
Experimental techniques
Solar wind
Spectroscopy

ABSTRACT

The surfaces of airless planetary bodies are subject to a barrage of charged particles, photons, and meteoroids. This high-energy space environment alters the surfaces and creates a tenuous atmosphere of ejected particles surrounding the celestial bodies. Experiments with well characterized analogue materials under controlled laboratory conditions are needed to interpret the observations of these atmospheres and improve composition models of such bodies. This study presents methods to create and analyze mineral powder pellets for ion irradiation experiments relevant for rocky planetary bodies including the Moon and Mercury. These include the pyroxenes diopside and enstatite, the plagioclase labradorite and the non-analogue pyroxenoid wollastonite. First ion irradiation experiments with diopside, enstatite and wollastonite pellets were performed under UHV with 4 keV He^+ at fluences of several 10^{21} ions m^{-2} (~100 and ~1000 years for Mercury and the Moon, respectively). The pellet's thermal IR reflectance properties were compared before and after irradiation showing monotonously shifting IR spectral features between $7-14$ μm towards higher wavelengths. For all irradiated pellets, Reststrahlen bands shifted by ~0.03 μm. Surface abrasion was found to remove the sputter effect, which is restricted to the top few tens of nm of the surface. Additionally, ion irradiation experiments were performed in a quartz crystal microbalance catcher setup, where the mass sputtered from pellets was monitored. This proves, that the presented sample preparation method allows the study of irradiation induced sputtering and surface alteration on the surfaces of rocky planets under laboratory conditions.

1. Introduction

Surfaces of atmosphere-free planetary bodies are constantly exposed to space weathering. Ongoing processes include micrometeorite impacts, thermal and photon-stimulated desorption, and solar wind induced sputtering (Plainaki et al., 2016; Bennett et al., 2013; Wurz and Lammer, 2003). These processes alter primarily the surface, but also create a collision-free exosphere, which is detectable with particle instruments onboard space probes such as LADEE, LRO, MESSENGER or the ongoing BepiColombo mission (Orsini et al., 2020; Milillo et al., 2020; Elphic et al., 2014; Paige et al., 2010; Solomon et al., 2001). The exosphere generated by space weathering is directly coupled to the planet surface and its chemical and mineralogical composition. Thus models of coupled systems are of interest to explain exosphere observations and interpret remote sensing data of the altered surface, particularly for planets without sample return such as Mercury (Rothery et al., 2020; Hiesinger et al., 2020; Alnussirat et al., 2018; Mura, 2012; Wurz et al., 2010). To bridge the gap between surface/exosphere models and space observations/sample return, planetary surface analogues are exposed to artificial space weathering and consecutively analysed.

The rocky surface of the Moon and Mercury are widely covered by an unconsolidated layer of solids, composed of fractured bedrock, referred to as regolith. The components range from single crystal and impact agglutinates to rock breccias and whole rock components (i.e., Heiken et al., 1991). To keep the sample parameters simple enough to understand the effects of irradiation experiments, these were performed on single minerals or derivatives thereof. The selection of analogue material for the Moon therefore includes minerals found in various mare and highland compositions known through sample return missions (e.g., Heiken et al., 1991, Table 1). For the surface of Mercury, the mineralogy

---

[*] Corresponding author.
E-mail address: noah.jaeggi@space.unibe.ch (N. Jäggi).

https://doi.org/10.1016/j.icarus.2021.114492
Received 16 October 2020; Received in revised form 22 March 2021; Accepted 18 April 2021
Available online 26 April 2021

Table 1
Lunar and Hermean surface mineral analogues based on literature data. The most prominent mineral groups are highlighted in bold.

For Mercury (McCoy et al., 2018)	For Moon (Heiken et al., 1991)
Pyroxene group	
Enstatite ($Mg_2Si_2O_6$)	Ferrosilite ($(Fe, Mg)_2Si_2O_6$)
Diopside ($CaMgSi_2O_6$)	Augite[†] ($(Ca, Mg, Fe, Al, Ti)_2(Si, Al)_2O_6$)
Plagioclase group $Na_xCa_{1-x}Al_{2-x}Si_{2+x}O_8$	
Labradorite to bytownite ($x \sim 0.5 - 0.2$)	Bytownite to anorthite ($x \sim 0.2 - 0$)
Olivine group $Mg_xFe_{2-x}SiO_4$	
Forsterite ($x = 2$)	Forsterite to fayalite ($x = 1.6 - 1.0$)
Oxide group	
	Ilmenite ($FeTiO_3$))
Sulfide group Niningerite (MgS)	

[†] While augite is a chemically extensive term, it is used specifically for (Fe,Ca, Mg)-pyroxene. With Al_2O_3 and TiO contents below 1 wt%, augites are representative of lunar highland pyroxenes, whereas mare basalt augites contain 2–3 wt% Al_2O_3 and TiO_2 (Heiken et al., 1991).

is inferred from remote sensing.

The data synopsis from MESSENGER's X-ray, gamma-ray and neutron spectrometer revealed fairly robust element ratios for provinces in the northern hemisphere of Mercury (Nittler et al., 2011). Based on this the estimated mineralogy for Mercury is dominated by pyroxene and plagioclase with minor olivine, and is thus similar to the Moon (McCoy et al., 2018; E. Vander Kaaden et al., 2017; Heiken et al., 1991). The prominent difference is the very low Fe-content of Mercury's silicates with <0.8 wt% FeO (Zolotov et al., 2013). In Table 1, a compilation of possible analogue materials for the Moon and Mercury is presented. The major rock forming minerals of Earth contain varying concentrations of Fe, which poses a challenge for the selection of minerals relevant for the low-Fe surface of Mercury. An example of an ideally Fe-free mineral is diopside from Zermatt, Switzerland, with ~2 wt% FeO, which was used in this study. To cover a FeO free end member next to diopside and enstatite, wollastonite is included, even though it is not an analogue for neither Moon nor Mercury. Further variations in composition among adequate analogues is not the focus of this study, but add an often neglected complexity.

This study focuses on space weathering by solar wind irradiation with typical ion energies of keV/nuc energies. This process is also referred to as sputtering and is initiated by energetic ions impacting a surface. The ions then lose all their energy through collisions with atoms and electrons in the rock- and regolith surface. (Nastasi et al., 1996; Sigmund, 1969). For Mercury and the Moon, the impinging ions are mainly solar wind H^+ and He^{2+} with contributions from heavier elements such as O^{5+}, O^{6+} and O^{7+} (Russell et al., 2016; von Steiger et al., 2000; Bame et al., 1975). Solar wind ions are the major contributor to space weathering on the Moon and Mercury. Furthermore the solar wind ion fluxes are constrained by MESSENGER measurements, opposed to micrometeorite fluxes, that are solely based on model calculations (e.g., Borin et al., 2009; Cintala, 1992). The penetration depth is a function of the ion energy and species, the impact angle, and the surface composition of the target. Defect formation by collision and the accumulation thereof gradually leads to amorphization and is capable of creating nanophase iron ($npFe^0$), as observed in the rims of lunar mineral grains (Pieters and Noble, 2016; Pieters et al., 2000; Keller and McKay, 1997).

The state of the art of sputter experiments is the irradiation of mineral thin films (Szabo et al., 2020; Szabo et al., 2018; Hijazi et al., 2017). To produce films suitable as planetary analogs, whole natural minerals are used as resource. The required size of the mineral used in the production of a thin film by Pulsed Laser Deposition (PLD) often exceeds that of naturally grown crystals and is thereby an important limiting factor. Using mineral pellets gives more flexibility in choosing samples for ion irradiation.

Another issue with PLD thin films made from silicates is the high solidus temperature of the minerals. Evaporation and consecutive deposition causes quenching and leads to glassy films (i.e., Hijazi et al., 2017). For this reason, potentially relevant aspects of sputtering, such as the influence of crystallinity and porosity, can only be studied with mineral powders or pellets representative of the physical, morphological, and mineralogical properties of planetary surfaces. Known behaviours of impacting ions on single crystals include channeling, which is the alignment of ions to the mineral lattice (Onderdelinden, 1966; Lindhard, 1965). Furthermore it is expected, that the material ejected by sputtering is decreasing with increasing porosity (Rodriguez-Nieva et al., 2011). How polycrystalline surfaces such as the regolith of Moon and Mercury behave is still unclear. For polycrystalline nonamorphizing materials such as bulk elemental metals it was shown however, that they behave different to single crystal samples and yields can be almost one order of magnitude larger (Schlueter et al., 2020). Apart from the expected differences caused by crystallinity and porosity, the use of mineral pellets in this regard takes into account that (1) minerals are the major components of Lunar soil samples, with an average of ~80 vol% (McKay et al., 1991, 2) mineral powders conserve stoichiometry, unlike thin-films produced with PLD, (Hijazi et al., 2017, 3) minerals and their powders have a long-range order and might show reduced formation of self-trapped excitons as suggested by Shluger and Stefanovich (1990), which are thought to be essential for sputter behavior caused by multiply charged ions Aumayr and Winter, 2004; Sporn et al., 1997). The use of mineral pellets is therefore of utmost interest when investigating sputter yields of planetary surfaces.

Surface properties and composition define the visual and infrared signal emitted by a planetary surface (i.e., Brunetto et al., 2020; Morlok et al., 2019; Pieters and Noble, 2016, and references therein). This study uses mid-infrared (MIR, 2.5–15 μm) reflectance spectra to investigate the effect that solar wind irradiation has on a pressed mineral pellet. The IR remote sensing data obtained by missions such as MESSENGER and the upcoming data from BepiColombo's MERTIS is, however, in the form of thermal emission infrared (TIR) (Morlok et al., 2019; Martin, 2018; Solomon et al., 2001). The conversion of emission to reflectance is described by Kirchhoff's law: Emission = 1 - Reflectance. The MIR spectra acquisition mode used in this study does, however, not allow a direct implementation of the law - to do so a hemispherical reflectance measurement would be necessary (Hapke, 2012; Thomson and Salisbury, 1993; Salisbury et al., 1994). Quantitative comparisons to TIR spectra are therefore not possible, however, the qualitative implications for IR features altered by irradiation is discussed and compared to previous studies using reflectance spectra.

Both reflectance and emission IR signals in the mid infrared are affected by a range of surface properties. These include high porosity being linked to grain size, causing reduced spectral contrast (Young et al., 2019; Salisbury and Wald, 1992), thermal alteration lowering reflectivity (Maturilli et al., 2017), large phase angles causing variations in the spectral shape (Maturilli et al., 2016; Varatharajan et al., 2019), a simulated lunar environment strongly changing feature locations (Lucey et al., 2017; Donaldson Hanna et al., 2017), solar wind irradiation strongly shifting features of meteorite-based powders (Lantz et al., 2017), and simulated micrometeorite impacts decreasing reflectance and slightly shifting features (Weber et al., 2020).

This study extends this list of parameters that influence IR spectra by acquiring reflectance MIR spectra for pellets exposed to solar wind He^+. The ions thereby have equivalent kinetic energy to their solar wind counterpart He^{2+}. The reasoning behind this is to omit the increased yield caused by potential sputtering, which is not well understood, and was shown to exceed simulated levels from purely kinetic SDTrimSP codes (Szabo et al., 2020; Szabo et al., 2018; Hijazi et al., 2017; Mutzke et al., 2019; von Toussaint et al., 2017; Mutzke et al., 2013). The effect of irradiation on MIR reflectance spectra are then compared to results of previous space weathering experiments as well as TIR spectra of Lunar soils (e.g., Brunetto et al., 2020; Weber et al., 2020; Lantz et al., 2017; Salisbury et al., 1997). The results contribute to the understanding of the combined effects of thermal alteration, grain size, phase angle, the measurement environment, micrometeorite impacts, and ion irradiation on the Lunar and Hermean surface TIR signal. The observations are furthermore discussed in the light of the interaction dept. of solar wind in mineral powders using SDTrimSP.

This study also presents methods for creating analogue samples for space weathering experiments with the use of minerals that can serve as reasonable analogues, representing the composition of planetary surfaces. The creation of very stable pressed mineral pellets is necessary because the exposure to simulated space weathering effects (such as irradiation, temperature cycles etc.) and the full characterization of the samples before and after these processes implies extensive handling and transport between different laboratory facilities. The alternative of using whole minerals is rejected, as pure end members are rare and generally too small to be used in a sputter setup similar to the one used for the thin film samples, and because a pellet has more in common with regolith than a single crystal. In the conclusions and outlook the future of mineral pellets, their use for determining representative MIR spectra and their potential to determine sputter yields through ion irradiation experiments is presented.

2. Methods

2.1. Samples and pre-irradiation characterization

To cover the better part of Lunar and Hermean mineralogy, the main focus of this study lies on the pyroxenes, i.e., enstatite and diopside, and the mid-Na and Ca plagioclase labradorite. Wollastonite, although not expected to be present on Mercury, serves as an ideal, Fe-free, Ca-silicate pyroxenoid for Mercury and was already studied by Szabo et al. (2020, 2018). In pellet form it is most resilient to handling and therefore poses the largest number of MIR spectra obtained in this study. The mineral samples are centimeter-sized, monocrystalline enstatite and labradorite, whereas diopside and wollastonite are decimeter sized and polycrystalline. Whole mineral element compositions were determined at the thin section scale and are listed in Table 2. For this purpose, electron backscatter imaging and X-ray mapping with energy dispersive spectrometry (EDS) was carried out using a ZEISS EVO 50 scanning electron microscope at the Institute of Geological Sciences of the University of Bern. An acceleration voltage of 20 kV and a beam current of 1.5–3 nA was used and the EDS data was corrected with the ZAF procedure using the software TEAMS version 2 from EDAX. EDS was only used prior to irradiation, as it is not suitable for determining non-isochemical surface alteration on the spatial scale of the ion irradiation penetration depth. The interaction volume of the electron beam is several μm deep, whereas alterations caused by irradiation only change the top few nm of the sample significantly.

Table 2
Pellet pressing method used to press mineral pellets and scanning electron microscopy chemical analysis of whole minerals.

	Wollastonite	Diopside	Enstatite	Labradorite[‡]
Method[†]	1,2	1,2	1,2	2
Oxides	wt%	wt%	wt%	wt%
SiO_2	52.22 ± 2.37	54.16 ± 0.18	55.47 ± 3.91	53.3
Al_2O_3	b.d.	b.d.	0.70 ± 0.50	30.0
FeO	b.d.	2.25 ± 0.52	5.22 ± 0.65	0.6
MgO	b.d.	20.55 ± 1.65	38.61 ± 3.25	b.d.
CaO	47.78 ± 1.37	23.04 ± 1.12	b.d.	12.6
Na_2O	b.d.	b.d.	b.d.	3.6
K_2O	b.d.	b.d.	b.d.	b.d.

[†] Pellet creation method necessary for a successful pellet. Either (1) pellet glued onto holder or (2) pellet pressed directly into holder.
[‡] Results from electron probe micro analysis from Wenk et al. (1965) with ≤1 % relative error.
Oxide contents below detection limits are labeled as such (b.d.). Labradorite from Surtsey with composition from Wenk et al. (1965).

2.2. Preparation of pellets

Because every sample was handled multiple times for measurements in Bern before and after the irradiation experiments were performed in Vienna, they had to be mechanically more robust than fluffy, planetary regolith. Pellets are not a perfect analogue to regolith, but they offer the best compromise between the required stability and planetary surfaces. The compressed property of the pellet is expected to influence solar wind irradiation results as the surface porosity of a pellet, analogous to regolith surface porosity, effectively reduces the sputter yield (Cassidy and Johnson, 2005).

Wollastonite, enstatite, diopside, and labradorite minerals were ground in a RETSCH agate disk mill to the point where the powder started to agglomerate. Extensive grinding of wollastonite was prohibited by needle formation and alignment in the disk-mill, due to well-developed cleavage. Similarly, minerals like labradorite with a hardness matching that of agate had to be crushed first. This was achieved using a tungsten carbide disk mill for a few seconds. In the case of wollastonite this was followed by manual milling in an agate mortar.

Grain size determination of powders was conducted in a particle size analyzer (Malvern Mastersizer 2000), with a small volume wet sample dispersion unit (Hydro 2000S). Small representative fractions of all mineral powders were dispersed in distilled water and irradiated by a laser. The dimensional information was derived from the resulting diffraction pattern. Size fractions of wollastonite, diopside, and enstatite were generated by wet sieving. The fractions for wollastonite were 150 − 60 μm, 60 − 30 μm, and <30 μm. For diopside and enstatite, the powder fractions were 60 − 30 μm and <30 μm. The large grain size fractions are representative of the coarse grained Lunar regolith whereas the finest grain size fraction are expected to represent Mercury's surface (Heiken et al., 1991).

Two methods for pressing pellets were employed. In the first method, pellets were pressed between two pistons and were extracted from the pellet press die (PD) mantle interior. For one pellet, ~0.3 g of material was used, and a pressure of 239 MPa was applied for ≥5 min. Using this method, wollastonite and diopside pellets could be pressed reliably. Enstatite and labradorite, however, remained delicate and broke easily when handled. In order to increase the stability of all successfully produced pellets, they were subsequently glued onto custom manufactured stainless steel back plates (Fig. 1(b)). An ultra-high vacuum (UHV) and high temperature secure carbon-based paste obtained from *Plano GmbH* was used. All pellets included in the post-irradiation MIR study are the products of this first method. (Method 1 in Table 2).

The first method turned out to be insufficient for the production of high stability pellets of enstatite and labradorite as well as large grain size fractions of Diopside due to their weak adhesion (Section 3.3). To achieve more stable pellets, a second method of pressing powder directly into holders was developed. For one pellet, ~0.03 *g* of material was used instead, reducing the amount of required material by over an order of magnitude. The pellets were pressed into holders without the use of a binder or glue by taking advantage of the intrinsic adhesion of the mineral powders (Fig. 1c). To counteract the low cohesion of mineral powders such as large grain size fractions of diopside, ~0.02 *g* of fine-grained wollastonite was pressed in the holder as a base, upon which ~0.01 *g* of the desired material was pressed. The pressure applied was reduced to 80 MPa to avoid sample holder deformation. This procedure

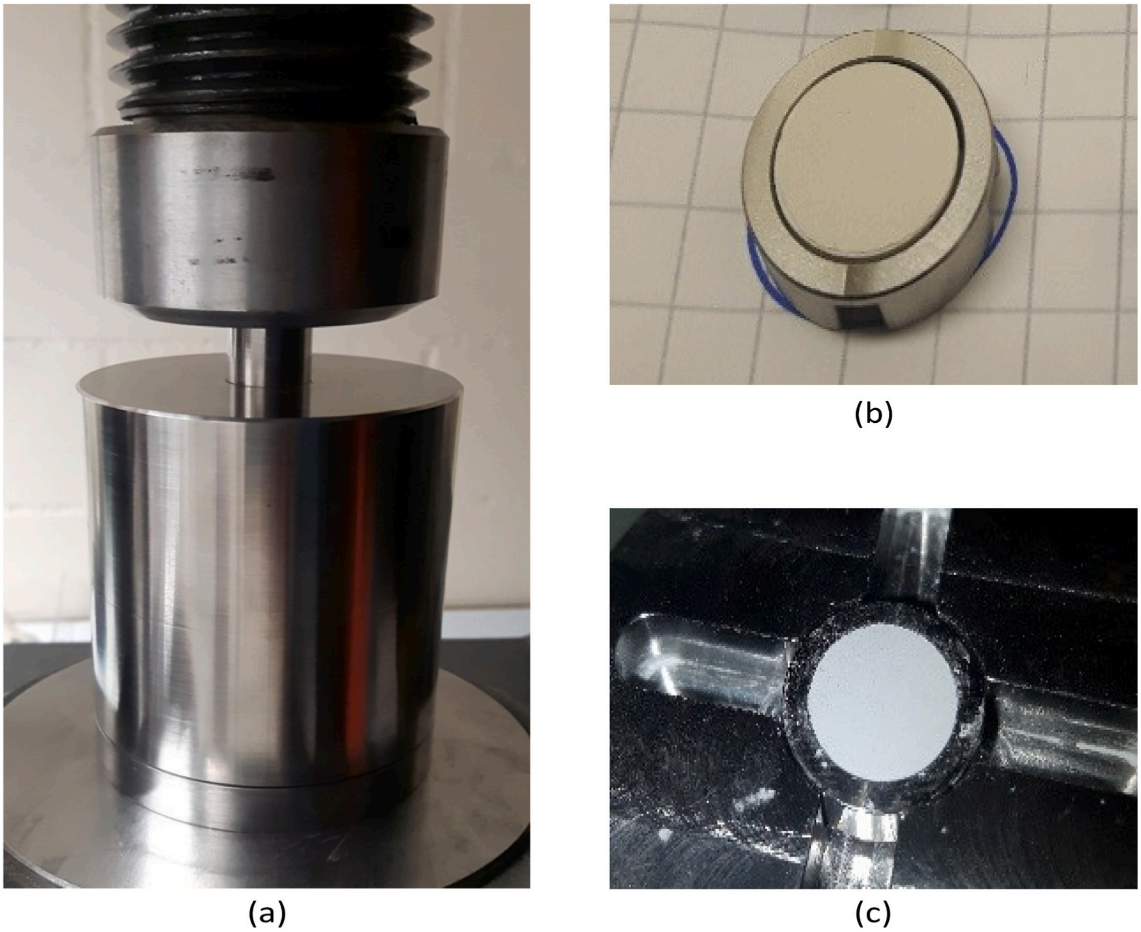

Fig. 1. (a) the custom pellet die in the press; (b) a pellet glued into its stainless steel holder by the means of vacuum secure glue and (c) a pellet pressed directly into a holder. Pellet diameters are 10 mm.

facilitates pellet extraction and minimizes pellet handling during creation. Powder fraction pellets of diopside used in the grain size reflectance MIR study are the products of this second method (Sections 3.4 & 3.5). In both methods, pellets were pressed in a custom made 10 mm diameter EXTRAMET EMT-210 alloy[1] PD and a 30 t hydraulic press (Fig. 1(a)).

2.3. Analysis methods before and after irradiation

Mid- to far-infrared micro reflectance measurements from 1.6 – 25 μm, covering the IR range of MERTIS, were done on pellets before and after irradiation using a Bruker Hyperion 2000 microscope attached to a Bruker Tensor FTIR spectrometer, at the Institute of Geological Sciences, University of Bern under ambient conditions. The FTIR is equipped with a Globar® infrared source, a liquid nitrogen-cooled mercury-cadmium-telluride detector, and a wire-grid polarizer. Backgrounds were regularly measured on a gold-coated slide, which has a reflectivity of about 100% for the selected wavelength range.

Reflectance spectra were collected with a total of 32 scans per measurement at a spectral resolution of 4 cm^{-1}. The locations of spectral features were reliably reproducible with an uncertainty of approximately 0.01 μm, therefore the position of spectral features are reported here to two decimal places. Background measurements through air were taken at 30 min intervals. Regular dry air purges of the chamber ensured low atmospheric contamination. MIR results were produced by taking spectra across the mineral pellet according to a predefined sampling map.

The predefined map covers the pellet in a cross from side to side with additional measuring points around the pellet center. The pellet holder was marked to maintain the same orientation and thus approximate location of the measurements following irradiation. The presented spectra are the average of the ten innermost data points located at and around the pellet center since this is the most homogeneously pressed and subsequently sputtered area. The spatial resolution of each point is ~25 μm; optical convolution effects are negligible (Ni and Zhang, 2008).

The extrema of each spectrum were determined using a python routine. The mean intensity of the ten measurements before and after irradiation is plotted and the variation in intensity is shown as a shaded area representing two standard deviations (2SD, Figs. 4 & 5). The difference of the extrema of each measured point before irradiation was compared to its equivalent after irradiation, averaged to a single shift. The mean and SD of an extrema location is reported together with the mean of all shifts at the given wavelength. The mean shift of a feature thereby often coincides in extent to one SD of the pre-irradiation feature position. A paired sample *t*-test was applied to compare the pre- and post-irradiation populations, finding *p*-values of <0.01 for all reported shifts, making them significant.

The choice of the MIR spectra range presented focuses on the location of the Christiansen feature (CF) around 8.5 μm, the Reststrahlen bands (RBs) between 8.5 – 12 μm and the transparency feature (TF) usually around 11 – 13 μm. The CF is an IR reflectance minimum, which is caused by the mineral refracting index matching the refracting

---

[1] From Manufacturer: 89.0% W, 10.0% Co, 1.0% other carbides.

index of the surrounding medium. RBs result from fundamental molecular vibrations caused by stretching of Si—O bonds (e.g., Salisbury, 1993). The TF is a wavelength range in which the mineral becomes optically thin as a result of a low absorption coefficient, with higher peaks in reflectance for samples with smaller grain-size (Donaldson Hanna et al., 2012; Salisbury and Wald, 1992). Mid-infrared spectroscopy of planetary analogs has shown that the TF is easily observed for powders with grain sizes $<$ 25 μm therefore its observation is only expected for small grain size fractions of diopside and wollastonite (Morlok et al., 2019; Donaldson Hanna et al., 2012). Under a simulated lunar environment only the TF of olivine was detectable, being the most apparent of all mineral TF in the $11-13$ μm range (Donaldson Hanna et al., 2012). Variance in reflectance intensity and changes in MIR features are used for interpretation of pellet properties affecting spectra. This study focuses on RB shifts as a measure of alteration while trying to reproduce physical property-dependent changes in RB contrast, as shown in other studies. The MIR reflectance measurements are shown and discussed within the wavelength range of MERTIS $7-14$ μm although they cannot be directly compared with TIR spectra of future BepiColombo or of the lunar soils analysed by Salisbury et al. (1997). Direct comparisons are, however, possible with MIR data from Brunetto et al. (2020) who simulated solar wind irradiation using He^+, but with an order of magnitude higher energy.

2.4. Irradiation experiments

Ion irradiation under vacuum conditions was performed at the ion beam facility at TU Wien (TUW). In a first step, it was necessary to verify that the method of powder sample preparation is appropriate for irradiation in the ion beam facility. To this end, several pellet samples were transported to TUW and irradiated with a 4 keV He beam with a typical flux of $10^{16}-10^{17}$ ions m^{-2} s^{-1} and fluences of several 10^{21} ions m^{-2}, representative for sputter experiments. The energy chosen reflects typical slow solar wind speeds of ~400 km s^{-1} and lies one order of magnitude below the extreme case scenario investigated by Lantz et al. (2017). For the fluxes of solar wind on the Moon and Mercury the fluence would correspond to an exposure of ~1000 and ~100 years (for fluxes see, e.g., Kallio et al., 2019; Winslow et al., 2017; McComas et al., 2009). This is applicable for the irradiation fluence used on the wollastonite and diopside pellets. During He irradiation of the enstatite pellet, the holder was partially sputtered as well, reducing the maximum fluence reached. Three wollastonite (WA1, WA2, WA3), one diopside and one enstatite pellet were irradiated. The samples were then sent back to University of Bern for MIR analysis.

The same facility was used for sputter experiments with PLD-produced films (Biber et al., 2020; Szabo et al., 2020; Szabo et al., 2018). In the case of the PLD method, the sample film was deposited on a quartz crystal microbalance (QCM), which directly measures the mass changes as the sample film is being irradiated. If a thick powder sample or pellet is used for sputter yield determination, the QCM must be mounted opposite of the sample to catch the ejecta from the irradiated sample (Fig. 2, Berger et al., 2017). The catcher QCM has a sensitive inner diameter of 7 mm, where a homogeneous deposition of material is assumed (Sauerbrey, 1959). The resulting area was used for calculating the total mass increase due to sputtered atoms sticking to the QCM. This technique demonstrably allows for measuring sputter yields as well as the angular distribution of sputtered particles (Stadlmayr et al., 2020). However, in order to avoid charging up of the insulating pellet samples, they have to be simultaneously irradiated with an electron flood source, which is installed in the setup at TUW.

To test the possibility of performing sputter yield measurements with mineral pellets in a catcher QCM-setup, a $\leq$ 30 μm fraction wollastonite pellet was irradiated by 2 keV Ar^+. Atomic force microscope images were taken to qualitatively compare the pellet surface roughness to glassy thin films. Mineral pellets thereby show an increased surface roughness (see appendix Fig. 8). To minimize stoichiometry changes on the catcher surface, a wollastonite coated QCM was used when irradiating the wollastonite pellet.

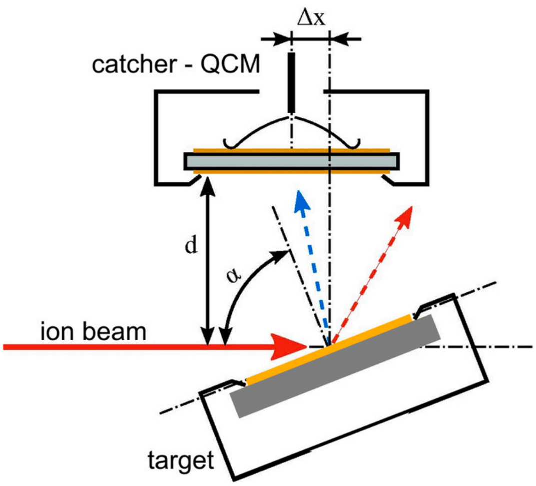

Fig. 2. Sputter setup with mineral pellet sample and quartz crystal microbalance (QCM) catcher. The mass change of the catcher QCM is a superposition of mass increase due to sticking of material ejected from the sample (blue arrow) and sputtering of the QCM itself due to reflected ions (red arrow). The distance d is measured from the target center and the catcher QCM. The angle of measured ejecta α is controlled by the offset Δx, describing the relative location of the catcher QCM to the sputtered target.For reference measurements, the target holder is replaced with a mineral coated QCM (Figure adapted from Berger et al., 2017). (For interpretation of the references to colour in this figure legend, the reader is referred to the web version of this article.)

3. Results

3.1. Chemical and physical properties

The weighted mean of the mineral powder grain diameters range from $23-28$ μm for diopside, enstatite and labradorite, and about 34 μm for wollastonite. The maxima in the grain size distributions lie below the weighted mean diameter, except for wollastonite, with a second, local maximum around 400 μm representing mineral needles still present after milling (Table 3).

3.2. First sputter yield results

Preliminary sputter experiments with 2 keV Ar^+ ions were performed in a catcher QCM setup (Sec. 2.4.). The sample was irradiated under an angle of incidence of 60° and at a distance d of 13 *mm*. The position Δx that coincides with a larger angle of the catching QCM relative to the target normal was varied to measure the material ejected in different directions (Fig. 2).

The mass increase of the catcher QCM per incident ion is shown in Fig. 3. A significant mass increase was resolved for all collection angles, which will allow the future determination of the total sputter yield.

Table 3
Grain sizes of mineral powders used.

	Wo	Di	En	Lab
$\overline{d}$	34.20	25.85	23.32	28.27
$d(0.1)$	1.73	1.73	1.64	2.10
$d(0.5)$	12.65	16.47	15.68	19.06
$d(0.9)$	77.35	60.55	60.71	68.8

Alongside the weighted mean grain diameter $\overline{d}$, characteristic grain sizes for three sample fractions are given in the form of diameter d larger or equal to 10%, 50%, and 90% of sample as $d(0.1)$, $d(0.5)$, and $d(0.9)$, respectively.

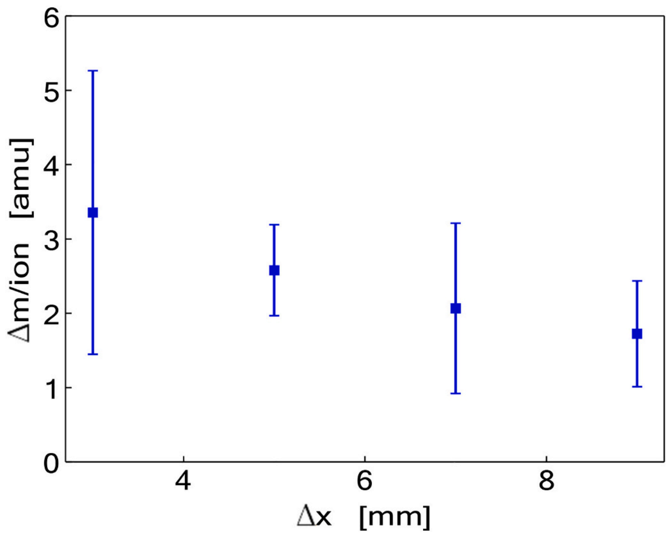

Fig. 3. Mass increase at the catcher QCM for various Δx positions when irradiating a wollastonite pellet with 2 *keV* Ar^+ ions under an angle of incidence of 60°. The distance was constant at $d = 13$ *mm*. The large uncertainties given originate from the small signal to background ratio.

However, the mass increase per ion is highest at small Δx, when catcher angles are close to the center of the ejecta distribution. Furthermore, the signal intensity is small compared to the background, leading to large uncertainties on the reported mass changes.

3.3. Pellet mechanical stability

The pellet stability shows large variations between the materials used. The pellet stabilities are presented in order of increasing Mohs hardness for unsieved and sieved powder pellets. Wollastonite powder resulted in the most durable pellets at any grain size. Enstatite had the tendency of creating faults during depressurization whereas slightly harder diopside showed comparable cohesion to wollastonite. Labradorite, the hardest mineral used, showed slightly worse adhesion than diopside, which could be connected to its intermediate CaO content compared to diopside and enstatite (Table 2).

When using grain fractions, the ≤ 30 μm fractions showed the highest cohesion for all minerals, as expected. The 30 − 60 μm fractions of diopside, enstatite, and labradorite exhibit strongly reduced adhesion. The trend of reduced adhesion coincides with the increasing mineral hardness. Generally, the lowest fractions of mineral powders do not allow for stable pellets apart from wollastonite and diopside.

3.4. IR spectra of blank and grain size fraction pellets

The effect of transportation on the MIR results was controlled using an un-irradiated wollastonite pellet blank (see appendix Fig. 6). The MIR spectra after transportation showed no statistically relevant alteration in terms of the position of features or reflectance loss, but a slightly higher variance on the reflectance measurements. There is, however, no TF or change thereof identifiable. Notable deviations between pre- and post-irradiation pellets were observed for the wollastonite pellet WA1 and the enstatite pellet. The former did suffer transport damage in the form of abrasion, whereas the latter was contaminated by pellet holder rim sputtering and deposition onto the pellet. The results of handling-affected pellets are presented and serve as an insight into indirect alteration processes such as abrasion and deposition of sputter ejecta.

The wollastonite and diopside pellets from powder fractions show a strong dependence on grain size (Fig. 4). In general, large grain size fractions resulted in a reduced spectral contrast, and large variance in reflectance. Loss in reflectance occurs at the high grain size spectra for diopside and the low grain size spectra of wollastonite. The wollastonite RBs at 8.92, 9.72 and 10.86 μm nearly disappear for the lowest grain size fraction of <30 μm, as expected. The reflectance loss also results in RB broadening, as seen next to the 9.72 and 10.32 μm RB. On the contrary for diopside band broadening is observed at large wavelengths for the <30 μm grain size fraction. The TF cannot be identified, however, the intensity of the TF region is increasing slightly as expected for smaller grain sizes.

High contrast RBs of wollastonite show minor shifts as the grain size is reduced from 60 to 150 μm to the <30 μm fraction. The 9.38 ± 0.01 μm RB and the pre-irradiation global maximum at 10.32 ± 0.01 μm both shift by 0.01 μm to higher wavelengths. In both cases the shift is similar to the 2SD reported on the RB location. Major shifts of ~0.03 μm are found for minor RBs, strongly affected by the increase in

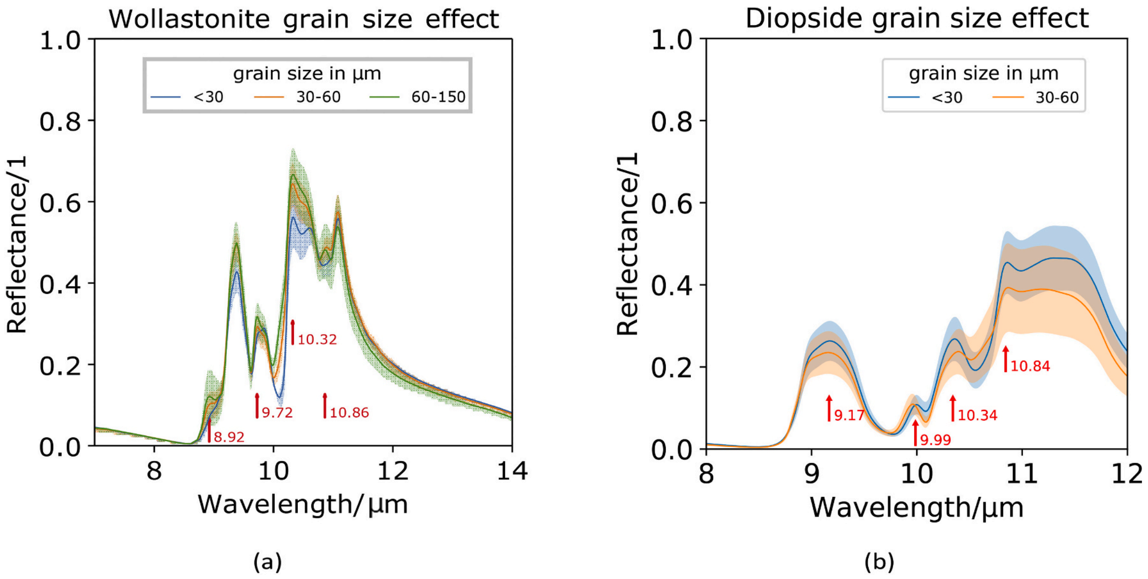

Fig. 4. Dependence of pellet reflectivity on grain size for pre-irradiation (a) wollastonite and (b) diopside. The largest grain size fraction resulted in the highest contrast between RBs, but also in the largest variations in TIR reflectivity (shaded area = 2SD). RB shifts are small or erratic towards lower and higher wavelengths for wollastonite and diopside.

spectral contrast such as the 9.73 ± 0.01, and 10.86 ± 0.01 μm RBs in Fig. 4. As those RBs are not persistent over all grain size spectra, they are not used to examine the effect of irradiation on the pellet spectra. The shift of the RBs at 8.93 ± 0.02 μm and 10.60 ± 0.01 μm, only visible in the 60 − 150 μm and <30 μm fraction spectra, respectively, are not reported due to the lack of distinguishable RBs in the spectra of other grain size fractions.

For diopside, the RBs have a low spectral contrast and show varying degrees of spectral shift when compared to the 30 − 60 μm grain size fraction spectra. The 9.18 ± 0.01 μm and the 9.99 ± 0.01 μm RB shift to higher wavelengths by 0.02 μm and 0.03 μm respectively. The 10.36 ± 0.01 μm RB, however, shifts to lower wavelengths by 0.03 μm, as does the global maxima at 10.86 ± 0.01 μm, which shows the smallest shift of 0.01 μm.

3.5. IR spectra of blank and irradiated pellets

Irradiated wollastonite, diopside and enstatite pellets show monotonous RB shifts towards higher wavelengths. An exception is the sputtered wollastonite pellet WA1, which had its top layers abraded during transport. Its MIR spectra strongly differ from the spectra of sputtered WA2 and WA3. The only RB shifts observed for WA1 are the 0.01 μm at the previous 9.234 ± 0.01 μm RB and the 0.02 μm at the global maximum 10.32 ± 0.01 μm, both towards higher wavelengths. The CF was located at 8.57 ± 0.01 μm and shifted 0.01 μm.

Both WA2 and WA3 show large shifts at all RBs after irradiation. The largest shifts of 0.05 μm and 0.03 μm were observed at the global maximum at 10.32 ± 0.01 μm and 10.32 ± 0.01 μm, respectively (Fig. 5(a)). Low contrast RBs with a high uncertainty on their position are not suited for comparison with pre-irradiation pellets but show similar or larger shifts than the high contrast RBs. The CF of WA2 does not shift within uncertainty 8.57 ± 0.01 μm, whereas for WA3 the shift

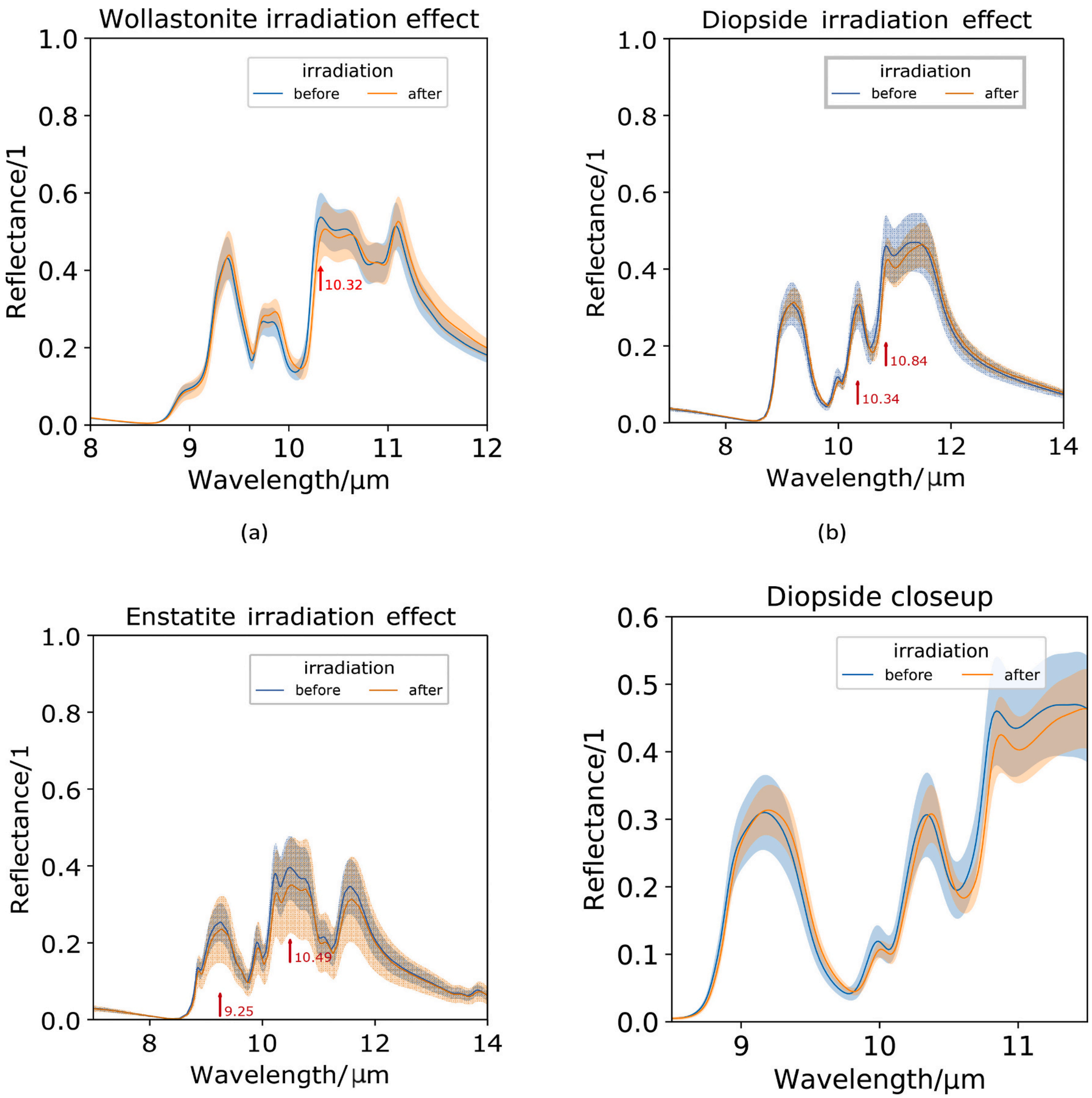

(a)

(b)

(c)

(d)

Fig. 5. Reststrahlen bands (RBs) of (a) wollastonite (WA2), (b) diopside, and (c) enstatite MIR reflectance data before and after irradiation. The wavelengths at which the largest and most notable shifts of RBs occur are highlighted by arrows and discussed in the text. All mineral pellets show a weak reflectance loss at the pre-irradiation global maximum. Enstatite further shows an increase in reflectance variance. All spectra show RB shifts towards higher wavelengths after irradiation. Filled areas show two standard deviations. A closeup of the diopside RBs is shown in (d), emphasizing the minor shifts caused by solar wind irradiation.

is 8.57 ± 0.02 μm + 0.02 μm.

On the irradiated diopside pellet the high contrast RBs shift by 0.02 − 0.04 μm to higher wavelengths (Fig. 5(b)). The largest shift of 0.04 μm was observed at the 10.34 ± 0.01 μm RB. Similar in extent is the 0.03 μm shift of the pre-irradiation global maximum, situated at 10.84 μm. The CF shifted from 8.49 ± 0.02 μm by 0.02 μm towards higher wavelengths.

Irradiation of enstatite result in the smallest shifts of high contrast RBs by 0.01 − 0.03 μm towards higher wavelengths (Fig. 5(c)). The increase of reflectance variation among the measurements is attributed to the sample holder being sputtered, resulting in deposits on the outer rim of the pellet surface. In terms of shifts, the pellet behaves similarly to wollastonite and diopside in that the major shift is 0.03 μm at the 9.25 ± 0.02 μm RB. The pre-irradiation maxima experienced the largest shift of 0.03 μm, however being a wide RB resulted in a large uncertainty on its location at 10.49 ± 0.01 μm. The CF shift by 0.01 μm from 8.44 ± 0.01 μm, similar in magnitude to the CF shift of the WA3 pellet.

The TF is not identifiable for any of the irradiated pellets, however, the TF region just slightly increases for wollastonite and diopside pellets after irradiation (Fig. 5(a) & (b)), suggesting a minute increase in the amount of fine grain material at the pellet surface. A similar behavior would be expected for enstatite, however the large variations in reflectance measurements do not allow for such a statement (Fig. 5(c)). Unlike spectra from pellets that stayed intact, the WA1 spectra shows significant reflectance loss. The TF region behaves, however, similarly to the irradiated wollastonite pellets, as it decreases less strongly relative to the RBs (Appendix, Fig. 7).

4. Discussion

Pellet properties such as composition, overall stability and grain size as well as the effect of solar wind irradiation are discussed in the light of IR results. The combined effects and their implications are then compared to previous Lunar focused studies.

4.1. Effect of composition

The composition of the irradiated pellets did not affect the extent of feature shifts in MIR spectra. This is seen in FeO-free wollastonite pellets with RB shifts analogue to FeO-bearing enstatite (for composition see Table 2). This indicates that intensity loss and major RB displacements in MIR spectra of diopside and enstatite are not connected to formation of nanophase iron, as it would be the case in NIR (e.g. Yang et al., 2017; Pieters and Noble, 2016; Kuhlman et al., 2015; Loeffler et al., 2009; Salisbury et al., 1997). The effect on the MIR spectra by solar wind irradiation is therefore likely caused by comminution and vitrification, altering the physical properties of the sample (Pieters and Noble, 2016; Nakamura et al., 2012; Salisbury et al., 1997). Pellet darkening was not visually observed on the irradiated pellets, with an exception of the experiment with the enstatite pellet, where the pellet holder was partially irradiated, depositing holder material onto the pellet rims. The consequences were (1) local darkening on the pellet rims, as seen in the large standard deviation on reflectance of the spectra after irradiation, and (2) a lower flux reaching the surface, which might have resulted in comparably low RB shifts.

4.2. Effect of grain size and surface roughness

It was shown by Salisbury and Wald (1992) that particle size and porosity are critically linked, which leads to the question how grain size affects MIR spectra. Small particle size leads to lowered spectral contrast, while reaching a high packing density restores RB contrast. As expected, lower pellet grain sizes negatively affected reflectance and spectral contrast in MIR, but RB positions are intrinsic to the material and not shifted (Salisbury and Wald, 1992; Lyon, 1965). The compression of powders is likely responsible for the less drastic reflectance differences in the grain size MIR spectra comparisons as shown in Fig. 4. The loss in spectral contrast is however seen in the merging of the wollastonite RBs near 10.86 μm at smaller grain size (Fig. 5). This merging of exactly two RBs could be an effect of mineral orientation, which changes when compressing very fine-grained wollastonite due to its good cleavage and its elongated fibrous crystal habit. This was shown for singly crystal olivine and is likely to occur when powders are used (Stojic et al., 2021; Reynard, 1991). It would be expected however, that averaging measuring points counteracts such orientation effects. No such strong effect was observed for diopside, likely due to the less pronounced cleavage that leads to more granular powder during grinding.

An unexpected observation was made in the grain size fraction measurements of diopside pellets, which do not follow the expected increase in spectral contrast with larger grain size. This might be connected to the destruction of diopside grains during pellet creation. The TF region being lower at large grain sizes however would suggest that the grain size is indeed larger. For irradiated pellets, the TF cannot be identified. Nevertheless, the TF region suggests a decrease in grain size for irradiated pellets, even for the abraded WA1 pellet. This could be tied to the transport process loosening weakly bond grains on the surface. No conclusive statement can be drawn, as the differences of the TF are marginal and could be caused by the small shifts of RBs.

Mean Lunar regolith grain-size lying between 40 and 100μm are significantly larger compared to the pellets used in this study (Heiken et al., 1991). The surface roughness is, however, still larger than glassy thin films used in prior sputter yield determination experiments. This is visible in AFM images (see appendix Fig. 8).

4.3. Effect of irradiation

The reported shifts of RBs and CFs are an order of magnitude below the 0.4 μm shifts reported in Brunetto et al. (2020). This can likely be explained by the ion beam penetration dept. The penetration depths of the 40 keV He^+ ion beam from Brunetto et al. (2020) under an angle of 0° are 278, 286, 349, and 380 nm for enstatite, diopside, wollastonite and labradorite, respectively, as calculated by SDTrimSP. The 4 keV beam from this study penetrates only about 22 nm into a diopside or enstatite crystal under an angle of 45°. The penetration in wollastonite and labradorite are slightly higher with 27 and 30 nm, respectively. The penetration dept. of ions in the minerals is thereby inversely proportional to the mineral density given in atoms per $Å^3$. The penetration depth of IR, however, is similar to that of a microprobe, which means >1 μm for 7 − 14 μm (Grzechnik et al., 1996).

Given this large interaction depth for IR, the shifts presented are interpreted to originate from a mixing of pristine material below an irradiated upper layer, as was proposed by Weber et al. (2020). The irradiation damage is reaching saturation in terms of damage per atom (dpa), which could add displacement of oxygen atoms to the proposed causes of irradiation-related CF shifts, together with vitrification and composition changes (e.g., Shluger and Stefanovich, 1990; Pieters and Noble, 2016). Furthermore, the irradiation damage of solar wind saturates under the given fluence. Therefore, the solar wind irradiation effect of He^+ on an IR spectrum will not exceed the shifts of 0.02 μm found in this study, which supports the proposition of Salisbury et al. (1997), that shifts ≤0.04 μm, as seen in the Apollo 16 soils samples, can be attributed to exposition to space weathering.

In relation to this, the extent of changes in CF position are expected to follow RB displacements as observed by Brunetto et al. (2020). In the present study, only some irradiated pellets show CF shifts of around 0.02 μm similar to the RB shifts. This is tentatively attributed to the lower interaction depth and a detection limit and not to an actual physical process.

Nash and Salisbury (1991) stated that vitrification does not cause shifts, or intensity loss, but loss of contrast. This latter coincides with the results of the present study, as in all pellets, the most intense RB lowered in intensity after irradiation, but the overall reflectance remained constant. Fitting the data of the CF positions in the Nash and Salisbury (1991) comparison plot of chemically identical crystalline powder and glass shows, however, that the CF does shift slightly. In Nash and Salisbury (1991), the Na-rich plagioclase end member albite shows a shift of ~0.04 μm towards lower wavelengths. This might be an indication of preferential sputtering of moderately volatile elements like Na, but it is unclear how this applies to minerals composed of refractory elements. This possibility of preferential sputtering will be further investigated once spectra of irradiated labradorite pellets become available.

An intense loss of MIR spectral contrast and strong shifts of features as shown in grain-size comparisons or shifts towards lower wavelengths were observed only to a minor extent on irradiated mineral pellets. This contradicts results from other studies where micrometeorite impacts were simulated using a pulsed laser, suggested to cause comminution and decompaction (Jiang et al., 2019; Weber et al., 2020). Note that the precision and representativeness of micrometeorite simulation by laser is limited by two major factors: (1) the fluxes of micrometeorites are not well known, nor is their chemical composition—the latter is generally disregarded when using a laser (i.e., Domingue et al., 2014, 2) realistic simulations of micrometeorite impacts require large dust accelerators which are sophisticated and rare instruments (i.e, Thomas et al., 2017).

4.4. Speculative effect of porosity and compression

For irradiation experiments, the behavior of pellets compared to loose powder is difficult to foretell, as the grains are comparably large and the porosity low compared to data available from tungsten fuzz irradiation experiments (Stadlmayr et al., 2020). For the MIR results, a larger porosity connected to unconsolidated powder would decrease spectral contrast. For the understanding of irradiation effects on spectral features, mineral pellets are the most valuable samples. They provide clear MIR spectral features, enable easy handling, and can be used in the same irradiation setup as designed for thin-films. The use of pellets is thus necessary for a step towards representative analogues and for direct comparisons with thin-film irradiation experiments.

4.5. Speculative effect of mechanical abrasion and pellet creation

The solar wind irradiation effect is likely to be lost by removing the layers affected by irradiation, not only due to transport damage, but also by surface altering effects on the Moon and Mercury. The MIR spectra of the WA1 pellet demonstrates the former, whereas all but two RBs did not show any significant shifts (Appendix Fig. 7). The dataset is, however, not sufficient to prove this statement as the shifts in MIR might not be genuine.

Effects of pellet creation on MIR spectra are less evident, although the creation of pellets from grain fractions suggests that grains that are >30 μm are preferentially lost in a pellet as they exhibit poor adhesion. Any mineral with high rigidity seems to experience less grain deformation, or cold welding, causing pellet instability. The large variance in pre-irradiation MIR reflectance of measurements taken on high hardness mineral pellets could represent this lack of homogeneous compression, as a lower packing density causes intensity loss (Salisbury and Wald, 1992).

4.6. Comparison to previous Lunar focused studies

For the pellets irradiated in this study, shifts in RBs are monotonous towards higher wavelengths and lie around 0.03 μm of displacement, similar to the CF shift reported in lunar soils (Salisbury et al., 1997). Furthermore, it was shown for LRO Diviner data, that the CF seems to have little sensitivity concerning physical and composition changes, but the RBs strongly alter between differently mature Lunar soils (Lucey et al., 2017). This is similar to the observed behavior of irradiated mineral pellets.

A difference is however the strong loss in reflectance, which is reminiscent of results from pulsed lasers used to simulate micrometeorite impacts (Weber et al., 2020). It is thus expected that the effect of micrometeorite impacts and contamination by other lithologies could override the effect of solar wind irradiation, however, more sophisticated experimental data would be necessary for alteration caused by micrometeorite impacts. Also, the timescales of the two studies are highly different. Weber et al. (2020) deposited a nominal energy of ~15 kJ/m^2 which translates to 300 Ma of micrometeorite impacts, which is five and six orders of magnitude larger respectively compared to the irradiation exposure time for Mercury and the Moon in this study.

4.7. Sputter yield results

First indirect measurements of sputter yields for a pressed wollastonite pellet using a QCM as catcher showed a similar trend in the angular distribution as was observed for flat, polycrystalline tungsten by Stadlmayr et al. (2020). A more detailed investigation with a direct measurement of angular dependence is necessary to use such sputter data for exosphere models, also in respect to the sample surface roughness (Küstner et al., 1999). Stadlmayr et al. (2020) also compared their flat samples with so-called tungsten fuzz, a tungsten structure with micrometer-size porosity. Using combined sputter measurements and simulations, they observed a drastic decrease in sputtering in contrast to the reference sample. However, Rodriguez-Nieva et al. (2011) did not observe a significant effect of nano-size porosity on the sputter yield in a molecular dynamic study, indicating, that the scale where porosity exists is crucial for sputter results. It is unclear in regard to the MIR results how this would affect the observed shifts. Locally, within one grain the penetration depth is not affected by increased porosity, however it is unclear which effects could either increase or decrease penetration depth and therefore the extent of shifts caused by the mix of sampled material in MIR.

5. Conclusions and outlook

The method of high-stability pellet creation presented here is appropriate for the entire sequence of pre- and post-analysis, irradiation and sputter yield experiments, and sample transport. This study further demonstrates the ability to use the produced pellets in UHV irradiation experiment chambers to obtain sputter yields using a catcher setup, and to investigate the resulting surface alteration in the context of space weathering. Resilient wollastonite, enstatite and diopside pellets are successfully irradiated, whereas more fragile labradorite pellets can only be produced with the second pellet creation method. Labradorite irradiation results were therefore excluded from MIR analysis.

Overall, a change in grain sizes causes only minor shifts in MIR spectra RB positions, whereas irradiation experiments lead to RB shifts of up to 0.04 μm similar to increasingly mature lunar regolith (Salisbury et al., 1997). The intensity of the observed shifts can be linked to the sputter agent energy in comparison with Brunetto et al. (2020); Lantz et al. (2017). Slow, 4 keV solar wind He^+ irradiation saturates within 1000 and 100 a exposure for the Moon and Mercury, respectively, which limits the irradiation effect on regolith and motivates the applied fluence for future studies. How multiply charged impacting ions with slow and fast solar wind energy would affect IR spectra is still unknown and is of interest for a future study.

First QCM catcher measurements were obtained. The observed general trend of mass increase on the catcher QCM as a function of ejecta angle agrees well with previous data for flat, polycrystalline tungsten samples (Stadlmayr et al., 2020). For the evaluation of sputter yields in a future study, an analysis of various parameters, including quartz properties and geometry of the system is necessary (as in Stadlmayr et al., 2020). Especially, the significant roughness of the mineral pellet, which can be seen in seen in AFM images, although better representing unconsolidated regolith, must not be neglected (Küstner et al., 1999) (see appendix Fig. 8).

This study demonstrates that mineral powder samples are very suitable for irradiation experiments. From the irradiation of these samples, it was found that solar wind could be responsible for the shift of IR features up to 0.04 μm. The next goal is to obtain effective sputter yields, to determined yield angle dependency, and to evaluate implantation behavior of impinging ions for the mineral groups most representative for the surfaces of the Moon and Mercury.

Declaration of Competing Interest

None.

Acknowledgements

Financial support has been provided by the Swiss National Science Foundation Fund (200021L_182771/1) as well as the Austrian Science Fund FWF (Project No. I 4101-N36) and by KKKÖ (Commission for the Coordination of Fusion research in Austria at the Austrian Academy of Sciences ÖAW).

Special thanks go to, located at the University of Bern, Stefano Spadaccia, Clément Feller, and Antoine Pommerol from WP (pycnometer), Alfons Berger from GEO (SEM analysis), Julien Reyes, and Jörg Hermann from GEO (TIR analysis), Alice Vho from GEO (sieving), Urs Eggenberger, and Christine Lemp from GEO (milling); Daniela Fischer from GIUB (grainsize analysis). From Bruker we would like to thank Hans-Christian Koch for his expertise on FTIR related questions. A special thanks goes to Beda Hofmann from the Natural History Museum of Bern for providing high quality diopside, bytownite, and labradorite mineral samples.

Appendix A. Transport effect MIR spectra

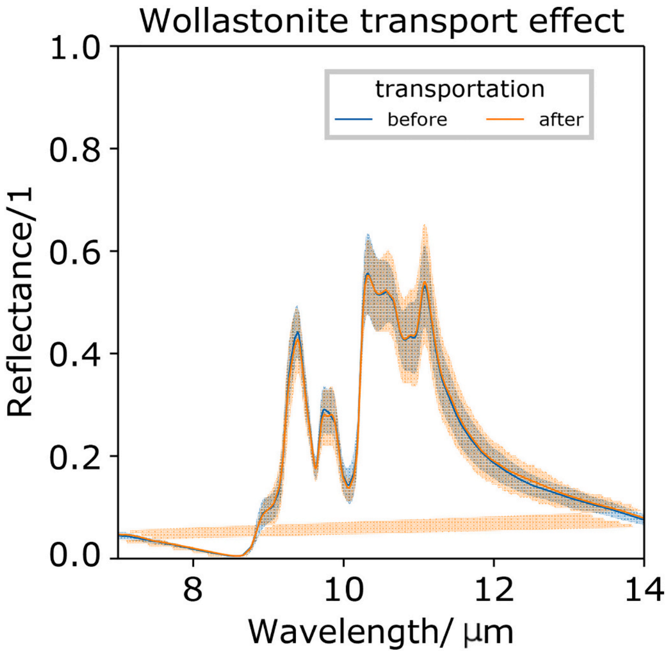

Fig. 6. TIR spectra of wollastonite blank showing a minor increase in reflectance variance after transportation.

Appendix B. Abrasion effect MIR spectra

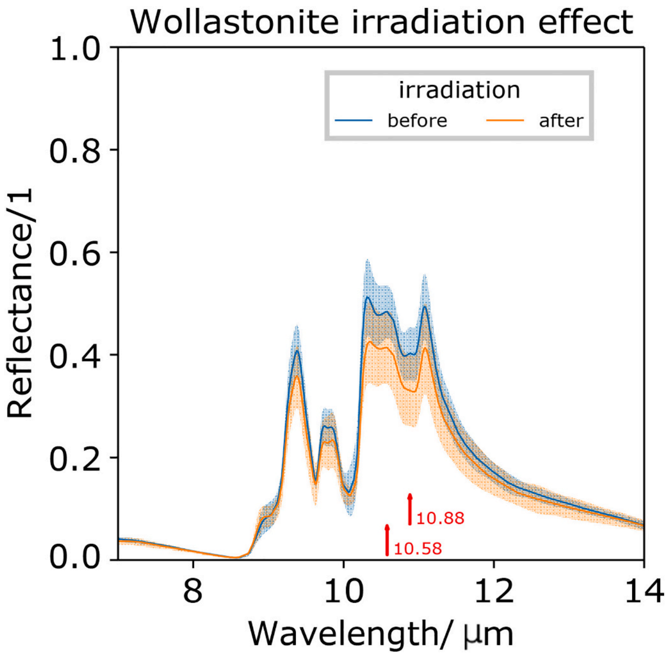

Fig. 7. MIR spectra of irradiated wollastonite showing a major decrease in reflectance variance after the top layer was abraded during transportation. Notable shifts of about 0.01 µm are only seen at the highlighted positions.

Appendix C. AFM images

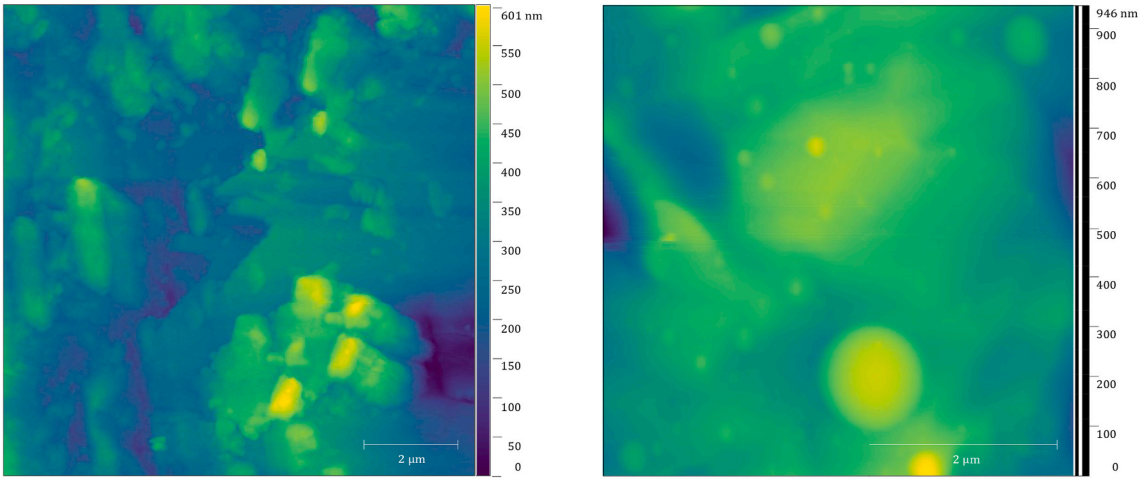

(a)

(b)

Fig. 8. AFM images of (a) irradiated wollastonite pellet with grain size <30 µm and of (b) a glassy wollastonite thin film as used in, e.g., Szabo et al. (2018).

References

Alnussirat, S.T., Barghouty, A.F., Edmunson, J.E., Sabra, M.S., Rickman, D.L., 2018. Contributions of solar-wind induced potential sputtering to the lunar surface erosion rate and it's exosphere. In: Nuclear Instruments and Methods in Physics Research Section B: Beam Interactions with Materials and Atoms, 420, pp. 33–39 https://www.sciencedirect.com/science/article/pii/S0168583X18300454?via{%}3Dihub{#}f0005. https://doi.org/10.1016/J.NIMB.2018.01.020.

Aumayr, F., Winter, H., 2004. Potential sputtering. In: Philosophical Transactions of the Royal Society of London. Series A: Mathematical, Physical and Engineering Sciences, 362, pp. 77–102. https://doi.org/10.1098/rsta.2003.1300.

Bame, S.J., Asbridge, J.R., Feldman, W.C., Montgomery, M.D., Kearney, P.D., 1975. Solar wind heavy ion abundances. Sol. Phys. 43, 463–473. https://doi.org/10.1007/BF00152368.

Bennett, C.J., Pirim, C., Orlando, T.M., 2013. Space-weathering of solar system bodies: a laboratory perspective. Chem. Rev. 113, 9086–9150.

Berger, B.M., Szabo, P.S., Stadlmayr, R., Aumayr, F., 2017. Sputtering measurements using a quartz crystal microbalance as a catcher. In: Nuclear Instruments and Methods in Physics Research Section B: Beam Interactions with Materials and Atoms, 406, pp. 533–537. https://www.sciencedirect.com/science/article/pii/S0168583X16305250. https://doi.org/10.1016/J.NIMB.2016.11.039.

Biber, H., Szabo, P.S., Jäggi, N., Wallner, M., Stadlmayr, R., Niggas, A., Moro, M.V., Primetzhofer, D., Nenning, A., Mutzke, A., 2020. A detailed look on the interaction of solar wind helium with Mercury's surface in the laboratory. In: EGU General Assembly Conference Abstracts, p. 9895.

Borin, P., Cremonese, G., Marzari, F., Bruno, M., Marchi, S., 2009. Statistical analysis of micrometeoroids flux on Mercury. Astron. Astrophys. 503, 259–264. https://www.aanda.org/articles/aa/abs/2009/31/aa12080-09/aa12080-09.html. https://doi.org/10.1051/0004-6361/200912080.

Brunetto, R., Lantz, C., Nakamura, T., Baklouti, D., Le Pivert-Jolivet, T., Kobayashi, S., Borondics, F., 2020. Characterizing irradiated surfaces using IR spectroscopy. Icarus 345, 113722. https://doi.org/10.1016/j.icarus.2020.113722.

Cassidy, T.A., Johnson, R.E., 2005. Monte Carlo model of sputtering and other ejection processes within a regolith. Icarus 176, 499–507 https://www.sciencedirect.com/science/article/pii/S0019103505000813?via{%}3Dihub{#}fig 001. https://doi.org/10.1016/J.ICARUS.2005.02.013.

Cintala, M.J., 1992. Impact-induced thermal effects in the lunar and Mercurian regoliths. J. Geophys. Res. 97, 947. https://doi.org/10.1029/91JE02207.

Domingue, D.L., Chapman, C.R., Killen, R.M., Zurbuchen, T.H., Gilbert, J.A., Sarantos, M., Benna, M., Slavin, J.A., Schriver, D., Trávníček, P.M., Orlando, T.M., Sprague, A.L., Blewett, D.T., Gillis-Davis, J.J., Feldman, W.C., Lawrence, D.J., Ho, G. C., Ebel, D.S., Nittler, L.R., Vilas, F., Pieters, C.M., Solomon, S.C., Johnson, C.L., Winslow, R.M., Helbert, J., Peplowski, P.N., Weider, S.Z., Mouawad, N., Izenberg, N. R., McClintock, W.E., 2014. Mercury's weather-beaten surface: understanding mercury in the context of lunar and asteroidal space weathering studies. Space Sci. Rev. 181, 121–214. https://doi.org/10.1007/s11214-014-0039-5.

Donaldson Hanna, K.L., Wyatt, M.B., Thomas, I.R., Bowles, N.E., Greenhagen, B.T., Maturilli, A., Helbert, J., Paige, D.A., 2012. Thermal infrared emissivity measurements under a simulated lunar environment: Application to the Diviner Lunar Radiometer Experiment. J. Geophys. Res. Planets 117.

Donaldson Hanna, K.L., Greenhagen, B.T., Patterson, W.R., Pieters, C.M., Mustard, J.F., Bowles, N.E., Paige, D.A., Glotch, T.D., Thompson, C., 2017. Effects of varying environmental conditions on emissivity spectra of bulk lunar soils: application to diviner thermal infrared observations of the moon. Icarus 283, 326–342. https://doi.org/10.1016/j.icarus.2016.05.034.

Elphic, R.C., Delory, G.T., Hine, B.P., Mahaffy, P.R., Horanyi, M., Colaprete, A., Benna, M., Noble, S.K., 2014. The Lunar Atmosphere and Dust Environment Explorer Mission. https://doi.org/10.1007/s11214-014-0113-z.

Grzechnik, A., Zimmermann, H.D., Hervig, R.L., King, P.L., McMillan, P.F., 1996. FTIR micro-reflectance measurements of the CO32- ion content in basanite and leucitite glasses. Contrib. Mineral. Petrol. 125, 311–318. https://doi.org/10.1007/s004100050224.

Hapke, B., 2012. Theory of reflectance and emittance spectroscopy. Cambridge university press.

Heiken, G.H., Vaniman, D.T., French, B.M. (Eds.), 1991. Lunar Sourcebook-a user's Guide to the Moon. Cambridge University Press, Cambridge, United Kingdom. http://adsabs.harvard.edu/abs/1991lsug.book.....H.

Hiesinger, H., Helbert, J., Alemanno, G., Bauch, K.E., D'Amore, M., Maturilli, A., Morlok, A., Reitze, M.P., Stangarone, C., Stojic, A.N., Varatharajan, I., Weber, I., Arnold, G., Banaszkiewicz, M., Bauch, K., Benkhoff, J., Bischoff, A., Blecka, M., Bowles, N., Calcutt, S., Colangeli, L., D'Amore, M., Erard, S., Fonti, S., Greenhagen, B.T., Groussain, O., Helbert, J., Hiesinger, H., Hirsch, H., Jahn, J., Killen, R., Knollenberg, J., Kührt, E., Lorenz, E., Mann, I., Mall, U., Maturilli, A., Morlok, A., Moroz, L., Peter, G., Rataj, M., Robinson, M., Skrbek, W., Spohn, T., Sprague, A., Stöffler, D., Stojic, A., Taylor, F., Varatharajan, I., Venus, H., Warrell, J., Walter, I., Weber, I., Witzke, A., Wöhler, C., 2020. Studying the composition and mineralogy of the Hermean surface with the mercury radiometer and thermal infrared spectrometer (MERTIS) for the BepiColombo Mission: an update. Space Sci. Rev. 216, 1–37. https://doi.org/10.1007/s11214-020-00732-4.

Hijazi, H., Bannister, M.E., Meyer, H.M., Rouleau, C.M., Meyer, F.W., 2017. Kinetic and potential sputtering of an anorthite-like glassy thin film. J. Geophys. Res. Planets 122, 1597–1609. https://doi.org/10.1002/2017JE005300.

Jiang, T., Zhang, H., Yang, Y., Hu, X., Ma, P., Sun, Y., Britt, D., Wang, W., Lu, X., Huang, J., Hsu, W., Mei, B., Wei, R., 2019. Bi-directional reflectance and polarization measurements of pulse-laser irradiated airless body analog materials. Icarus 331, 127–147. https://doi.org/10.1016/j.icarus.2019.05.022.

Kallio, E., Dyadechkin, S., Wurz, P., Khodachenko, M., 2019. Space weathering on the moon: Farside-nearside solar wind precipitation asymmetry. Planet. Space Sci. 166, 9–22 https://www.sciencedirect.com/science/article/pii/S0032063318301818?via{%}3Dihub{#}fig 1. https://doi.org/10.1016/J.PSS.2018.07.013.

Keller, L.P., McKay, D.S., 1997. The nature and origin of rims on lunar soil grains. Geochim. Cosmochim. Acta 61, 2331–2341. https://doi.org/10.1016/s0016-7037(97)00085-9.

Kuhlman, K.R., Sridharan, K., Kvit, A., 2015. Simulation of solar wind space weathering in orthopyroxene. Planet. Space Sci. 115, 110–114. https://www.sciencedirect.com/science/article/pii/S0032063315001075. https://doi.org/10.1016/J.PSS.2015.04.003.

Küstner, M., Eckstein, W., Hechtl, E., Roth, J., 1999. Angular dependence of the sputtering yield of rough beryllium surfaces. J. Nucl. Mater. 265, 22–27 https://www.sciencedirect.com/science/article/pii/S0022311598006485{#}FIG 1. https://doi.org/10.1016/S0022-3115(98)00648-5.

Lantz, C., Brunetto, R., Barucci, M.A., Fornasier, S., Baklouti, D., Bourçois, J., Godard, M., 2017. Ion irradiation of carbonaceous chondrites: a new view of space weathering on primitive asteroids. Icarus 285, 43–57. https://doi.org/10.1016/j.icarus.2016.12.019.

Lindhard, J., 1965. Influence of crystal lattice on motion of energetic charged particles. In: Matematisk-fysiske meddelelser Kongelige Danske Videnskabernes Selskab, 34. https://www.osti.gov/biblio/4536390.

Loeffler, M.J., Dukes, C.A., Baragiola, R.A., 2009. Irradiation of olivine by 4 keV He ⁺ : simulation of space weathering by the solar wind. J. Geophys. Res. 114, E03003. https://doi.org/10.1029/2008JE003249.

Lucey, P.G., Greenhagen, B.T., Song, E., Arnold, J.A., Lemelin, M., Hanna, K.D., Bowles, N.E., Glotch, T.D., Paige, D.A., 2017. Space weathering effects in diviner lunar radiometer multispectral infrared measurements of the lunar Christiansen feature: characteristics and mitigation. Icarus 283, 343–351. https://doi.org/10.1016/j.icarus.2016.05.010.

Lyon, R.J., 1965. Analysis of rocks by spectral infrared emission (8 to 25 microns). Econ. Geol. 60, 715–736. https://doi.org/10.2113/gsecongeo.60.4.715.

Martin, D.J.P., 2018. IR Spectroscopy of Planetary Regolith Analogues, Lunar Meteorites, and Apollo Soils. The University of Manchester (United Kingdom).

Maturilli, A., Helbert, J., Ferrari, S., D'Amore, M., 2016. On the effect of emergence angle on emissivity spectra: application to small bodies science of solar system materials examined from Hayabusa and future missions (II) 7. In: Planetary science. Earth, Planets and Space, 68, p. 84. https://doi.org/10.1186/s40623-016-0464-7.

Maturilli, A., Helbert, J., Varatharajan, I., Hiesinger, H., 2017. Emissivity spectra of analogue materials at Mercury P-T conditions. In: 48th Lunar and Planetary Science Conference, held 20-24 March 2017, at The Woodlands, Texas. LPI Contribution No. 1964, id.1427 48. http://adsabs.harvard.edu/abs/2017LPI....48.1427M.

McComas, D.J., Allegrini, F., Bochsler, P., Bzowski, M., Christian, E.R., Crew, G.B., DeMajistre, R., Fahr, H., Fichtner, H., Frisch, P.C., Funsten, H.O., Fuselier, S.A., Gloeckler, G., Gruntman, M., Heerikhuisen, J., Izmodenov, V., Janzen, P., Knappenberger, P., Krimigis, S., Kucharek, H., Lee, M., Livadiotis, G., Livi, S., MacDowall, R.J., Mitchell, D., Möbius, E., Moore, T., Pogorelov, N.V., Reisenfeld, D., Roelof, E., Saul, L., Schwadron, N.A., Valek, P.W., Vanderspek, R., Wurz, P., Zank, G. P., 2009. Global observations of the interstellar interaction from the interstellar boundary explorer (IBEX). Science (New York, N.Y.) 326, 959–962.

McCoy, T.J., Peplowski, P.N., McCubbin, F.M., Weider, S.Z., 2018. The geochemical and mineralogical diversity of mercury. In: Solomon, S.C., Nittler, L.R., Anderson, B.J. (Eds.), Mercury: The View after MESSENGER, 21. Cambridge University Press, Cambridge, United Kingdom, pp. 176–190. https://doi.org/10.1017/9781316650684 chapter 7.

McKay, D.S., Heiken, G.H., Basu, A., Blanford, G., Simon, S.B., Reedy, R., French, B.M., Papike, J., 1991. The lunar regolith. In: Heiken, G.H., Vaniman, D.T., French, B.M (Eds.), Lunar Sourcebook-a user's Guide to the Moon. Cambridge University Press, Cambridge, United Kingdom, pp. 285–356 chapter 7. http://adsabs.harvard.edu/abs/1991lsug.book.....H.

Milillo, A., Fujimoto, M., Murakami, G., Benkhoff, J., Zender, J., Aizawa, S., Dósa, M., Griton, L., Heyner, D., Ho, G., Imber, S.M., Jia, X., Karlsson, T., Killen, R.M., Laurenza, M., Lindsay, S.T., McKenna-Lawlor, S., Mura, A., Raines, J.M., Rothery, D. A., André, N., Baumjohann, W., Berezhnoy, A., Bourdin, P.A., Bunce, E.J., Califano, F., Deca, J., de la Fuente, S., Dong, C., Grava, C., Fatemi, S., Henri, P., Ivanovski, S.L., Jackson, B.V., James, M., Kallio, E., Kasaba, Y., Kilpua, E., Kobayashi, M., Langlais, B., Leblanc, F., Lhotka, C., Mangano, V., Martindale, A., Massetti, S., Masters, A., Morooka, M., Narita, Y., Oliveira, J.S., Odstrcil, D., Orsini, S., Pelizzo, M.G., Plainaki, C., Plaschke, F., Sahraoui, F., Seki, K., Slavin, J.A., Vainio, R., Wurz, P., Barabash, S., Carr, C.M., Delcourt, D., Glassmeier, K.H., Grande, M., Hirahara, M., Huovelin, J., Korablev, O., Kojima, H., Lichtenegger, H., Livi, S., Matsuoka, A., Moissl, R., Moncuquet, M., Muinonen, K., Quèmerais, E., Saito, Y., Yagitani, S., Yoshikawa, I., Wahlund, J.E., 2020. Investigating Mercury's environment with the two-spacecraft BepiColombo mission. Space Sci. Rev. 216, 1–78. https://doi.org/10.1007/s11214-020-00712-8.

Morlok, A., Klemme, S., Weber, I., Stojic, A., Sohn, M., Hiesinger, H., Helbert, J., 2019. Mid-infrared spectroscopy of planetary analogs: a database for planetary remote sensing. Icarus 324, 86–103. https://doi.org/10.1016/j.icarus.2019.02.010.

Mura, A., 2012. Loss rates and time scales for sodium at mercury. Planet. Space Sci. 63-64, 2–7 https://www.sciencedirect.com/science/article/pii/S0032063311002728{#}f0015. https://doi.org/10.1016/J.PSS.2011.08.012.

Mutzke, A., Schneider, R., Bandelow, G., 2013. SDTrimSP-2D: Simulation of Particles Bombarding on a Two Dimensional Target-Version 2.0. http://hdl.handle.net/11858/00-001M-0000-0026-E06F-E.

Mutzke, A., Schneider, R., Eckstein, W., Dohmen, R., Schmid, K., von Toussaint, U., Badelow, G., 2019. SDTrimSP Version 6.00.

Nakamura, E., Makishima, A., Moriguti, T., Kobayashi, K., Tanaka, R., Kunihiro, T., Tsujimori, T., Sakaguchi, C., Kitagawa, H., Ota, T., Yachi, Y., Yada, T., Abe, M., Fujimura, A., Ueno, M., Mukai, T., Yoshikawa, M., Kawaguchi, J., 2012. Space environment of an asteroid preserved on micrograins returned by the Hayabusa spacecraft. Proc. Natl. Acad. Sci. U. S. A. 109, E624–E629. https://doi.org/10.1073/pnas.1116236109.

Nash, D.B., Salisbury, J.W., 1991. Infrared reflectance spectra (2.2-15 μm) of plagioclase feldspars. Geophys. Res. Lett. 18, 1151–1154. https://doi.org/10.1029/91GL01008.

Nastasi, M., Michael, N., Mayer, J., Hirvonen, J.K., James, M., 1996. Ion-Solid Interactions: Fundamentals and Applications. Cambridge University Press.

Ni, H., Zhang, Y., 2008. H2O diffusion models in rhyolitic melt with new high pressure data. Chem. Geol. 250, 68–78. https://www.sciencedirect.com/science/article/pii/S0009254108000806. https://doi.org/10.1016/J.CHEMGEO.2008.02.011.

Nittler, L.R., Starr, R.D., Weider, S.Z., McCoy, T.J., Boynton, W.V., Ebel, D.S., Ernst, C.M., Evans, L.G., Goldsten, J.O., Hamara, D.K., Lawrence, D.J., McNutt, R.L., Schlemm, C. E., Solomon, S.C., Sprague, A.L., 2011. The major-element composition of Mercury's surface from MESSENGER X-ray spectrometry. Science 333, 1847–1850. https://doi.org/10.1126/science.1211567.

Onderdelinden, D., 1966. The influence of channeling on cu single-crystal sputtering. Appl. Phys. Lett. 8, 189–190. https://doi.org/10.1063/1.1754548.

Orsini, S., Livi, S., Lichtenegger, H., Barabash, S., Milillo, A., Angelis, E.D., Phillips, M., Laky, G., 2020. SERENA : particle instrument suite for Sun-mercury interaction insights on-board BepiColombo. Space Sci. Rev. 217, 49.

Paige, D.A., Foote, M.C., Greenhagen, B.T., Schofield, J.T., Calcutt, S., Vasavada, A.R., Preston, D.J., Taylor, F.W., Allen, C.C., Snook, K.J., 2010. The lunar reconnaissance orbiter diviner lunar radiometer experiment. Space Sci. Rev. 150, 125–160.

Pieters, C.M., Noble, S.K., 2016. Space weathering on airless bodies. J. Geophys. Res. Planets 121, 1865–1884. https://doi.org/10.1002/2016JE005128@10.1002/(ISSN)2169-9100.JGRE25.

Pieters, C.M., Taylor, L.A., Noble, S.K., Keller, L.P., Hapke, B., Morris, R.V., Allen, C.C., McKAY, D.S., Wentworth, S., 2000. Space weathering on airless bodies: Resolving a mystery with lunar samples. Meteorit. Planet. Sci. 35, 1101–1107. https://doi.org/10.1111/j.1945-5100.2000.tb01496.x.

Plainaki, C., Lilensten, J., Radioti, A., Andriopoulou, M., Milillo, A., Nordheim, T.A., Dandouras, I., Coustenis, A., Grassi, D., Mangano, V., Massetti, S., Orsini, S., Lucchetti, A., 2016. Planetary space weather: scientific aspects and future perspectives. J. Space Weather Space Clim. 6, A31. https://doi.org/10.1051/swsc/2016024.

Reynard, B., 1991. Single-crystal infrared reflectivity of pure Mg2SiO2 forsterite and (Mg0.86,Fe0.14)2SiO4 olivine - New data and a reappraisal. Phys. Chem. Miner. 18, 19–25. https://doi.org/10.1007/BF00199039.

Rodriguez-Nieva, J.F., Bringa, E.M., Cassidy, T.A., Johnson, R.E., Caro, A., Fama, M., Loeffler, M.J., Baragiola, R.A., Farkas, D., 2011. Sputtering from a porous material by penetrating ions. Astrophys. J. Lett. 743, 5. http://lammps.sandia.gov. https://doi.org/10.1088/2041-8205/743/1/L5.

Rothery, D.A., Massironi, M., Alemanno, G., Barraud, O., Besse, S., Bott, N., Brunetto, R., Bunce, E., Byrne, P., Capaccioni, F., Capria, M.T., Carli, C., Charlier, B., Cornet, T., Cremonese, G., D'Amore, M., De Sanctis, M.C., Doressoundiram, A., Ferranti, L., Filacchione, G., Galluzzi, V., Giacomini, L., Grande, M., Guzzetta, L.G., Helbert, J., Heyner, D., Hiesinger, H., Hussmann, H., Hyodo, R., Kohout, T., Kozyrev, A., Litvak, M., Lucchetti, A., Malakhov, A., Malliband, C., Mancinelli, P., Martikainen, J., Martindale, A., Maturilli, A., Milillo, A., Mitrofanov, I., Mokrousov, M., Morlok, A., Muinonen, K., Namur, O., Owens, A., Nittler, L.R., Oliveira, J.S., Palumbo, P., Pajola, M., Pegg, D.L., Penttilä, A., Politi, R., Quarati, F., Re, C., Sanin, A., Schulz, R., Stangarone, C., Stojic, A., Tretiyakov, V., Väisänen, T., Varatharajan, I., Weber, I., Wright, J., Wurz, P., Zambon, F., 2020. Rationale for BepiColombo studies of Mercury's surface and composition. Space Sci. Rev. 216, 66. https://doi.org/10.1007/s11214-020-00694-7.

Russell, C.T., Luhmann, J.G., Strangeway, R.J., 2016. Space Physics: An Introduction. Cambridge University Press.

Salisbury, J.W., 1993. Mid-infrared spectroscopy: Laboratory data. In: Remote Geochemical Analysis: Elemental and Mineralogical Composition, p. 618.

Salisbury, J.W., Wald, A., 1992. The role of volume scattering in reducing spectral contrast of reststrahlen bands in spectra of powdered minerals. Icarus 96, 121–128. https://doi.org/10.1016/0019-1035(92)90009-V.

Salisbury, John W., Wald, Andrew, D'Aria, Dana M., 1994. Thermal-infrared remote sensing and Kirchhoff's law: 1. Laboratory measurements. J. Geophys. Res. Solid Earth 99, 11897–11911. https://doi.org/10.1029/93JB03600.

Salisbury, J.W., Basu, A., Fischer, E.M., 1997. Thermal infrared spectra of lunar soils. Icarus 130, 125–139. https://doi.org/10.1006/icar.1997.5809.

Sauerbrey, G., 1959. Verwendung von Schwingquarzen zur Wägung dünner Schichten und zur Mikrowägung. Z. Phys. 155, 206–222. https://doi.org/10.1007/BF01337937.

Schlueter, K., Nordlund, K., Hobler, G., Balden, M., Granberg, F., Flinck, O., Da Silva, T. F., Neu, R., 2020. Absence of a crystal direction regime in which sputtering corresponds to amorphous material. Phys. Rev. Lett. 125, 225502. https://doi.org/10.1103/PhysRevLett.125.225502.

Shluger, A., Stefanovich, E., 1990. Models of the self-trapped exciton and nearest-neighbor defect pair in SiO 2. Phys. Rev. B 42, 9664–9673. https://doi.org/10.1103/PhysRevB.42.9664.

Sigmund, P., 1969. Theory of sputtering. I. Sputtering yield of amorphous and polycrystalline targets. Phys. Rev. 184, 383–416. https://doi.org/10.1103/PhysRev.184.383 (arXiv:PhysRev.184.383).

Solomon, S.C., McNutt, R.L., Gold, R.E., Acuña, M.H., Baker, D.N., Boynton, W.V., Chapman, C.R., Cheng, A.F., Gloeckler, G., Head, J.W., Krimigis, S.M., McClintock, W.E., Murchie, S.L., Peale, S.J., Phillips, R.J., Robinson, M.S., Slavin, J. A., Smith, D.E., Strom, R.G., Trombka, J.I., Zuber, M.T., 2001. The MESSENGER mission to mercury: scientific objectives and implementation. Planet. Space Sci. 49, 1445–1465. https://doi.org/10.1016/S0032-0633(01)00085-X.

Sporn, M., Libiseller, G., Neidhart, T., Schmid, M., Aumayr, F., Winter, H.P., Varga, P., Grether, M., Niemann, D., Stolterfoht, N., 1997. Potential sputtering of clean SiO2 by slow highly charged ions. Phys. Rev. Lett. 79, 945–948. https://doi.org/10.1103/PhysRevLett.79.945.

Stadlmayr, R., Szabo, P.S., Mayer, D., Cupak, C., Dittmar, T., Bischoff, L., Möller, S., Rasiński, M., Wilhelm, R.A., Möller, W., Aumayr, F., 2020. Sputtering of nanostructured tungsten and comparison to modelling with TRI3DYN. J. Nucl. Mater. 532, 152019. https://doi.org/10.1016/j.jnucmat.2020.152019.

Stojic, A.N., Morlok, A., Tollan, P., Kohout, T., Hermann, J., Weber, I., Moreau, J.G., Hiesinger, H., Sohn, M., Bauch, K.E., Reitze, M.P., Helbert, J., 2021. A shock recovery experiment and its implications for Mercury's surface: the effect of high pressure on porous olivine powder as a regolith analog. Icarus 357, 114162. https://doi.org/10.1016/j.icarus.2020.114162.

Szabo, P.S., Chiba, R., Biber, H., Stadlmayr, R., Berger, B.M., Mayer, D., Mutzke, A., Doppler, M., Sauer, M., Appenroth, J., Fleig, J., Foelske-Schmitz, A., Hutter, H., Mezger, K., Lammer, H., Galli, A., Wurz, P., Aumayr, F., 2018. Solar wind sputtering of wollastonite as a lunar analogue material – comparisons between experiments and simulations. Icarus 314, 98–105.

Szabo, P.S., Biber, H., Jäggi, N., Brenner, M., Weichselbaum, D., Niggas, A., Stadlmayr, R., Primetzhofer, D., Nenning, A., Mutzke, A., Sauer, M., Fleig, J., Foelske-Schmitz, A., Mezger, K., Lammer, H., Galli, A., Wurz, P., Aumayr, F., 2020. Dynamic potential sputtering of lunar analog material by solar wind ions. Astrophys. J. 891, 100. https://doi.org/10.3847/1538-4357/ab7008.

Thomas, E., Simolka, J., DeLuca, M., Horányi, M., Janches, D., Marshall, R.A., Munsat, T., Plane, J.M., Sternovsky, Z., 2017. Experimental setup for the laboratory investigation of micrometeoroid ablation using a dust accelerator. Rev. Sci. Instrum. 88, 034501. https://doi.org/10.1063/1.4977832.

Vander Kaaden, K.E., McCubbin, F.M., Nittler, L.R., Peplowski, P.N., Weider, S.Z., Frank, E.A., McCoy, T.J., 2017. Geochemistry, mineralogy, and petrology of boninitic and komatiitic rocks on the mercurian surface: Insights into the mercurian mantle. Icarus 285, 155–168 https://www.sciencedirect.com/science/article/pii/S0019103516303116{#}fig0001 https://linkinghub.elsevier.com/retrieve/pii/S0019103516303116. https://doi.org/10.1016/j.icarus.2016.11.041.

Varatharajan, I., Maturilli, A., Helbert, J., Alemanno, G., Hiesinger, H., 2019. Spectral behavior of sulfides in simulated daytime surface conditions of mercury: supporting past (MESSENGER) and future missions (BepiColombo). Earth Planet. Sci. Lett. 520, 127–140. https://doi.org/10.1016/j.epsl.2019.05.020.

von Steiger, R., Schwadron, N.A., Fisk, L.A., Geiss, J., Gloeckler, G., Hefti, S., Wilken, B., Wimmer-Schweingruber, R.R., Zurbuchen, T.H., 2000. Composition of quasi-stationary solar wind flows from Ulysses/solar wind ion composition spectrometer. J. Geophys. Res. Space Physics 105, 27217–27238. https://doi.org/10.1029/1999JA000358.

von Toussaint, U., Mutzke, A., Manhard, A., 2017. Sputtering of rough surfaces: a 3D simulation study. Phys. Scr. T170, 014056. http://stacks.iop.org/1402-4896/2017/i=T170/a=014056?key=crossref.54a755fcf210fc637a4c40aaeacbc2f3. https://doi.org/10.1088/1402-4896/aa90be.

Weber, I., Stojic, A.N., Morlok, A., Reitze, M.P., Markus, K., Hiesinger, H., Pavlov, S.G., Wirth, R., Schreiber, A., Sohn, M., Hübers, H.W., Helbert, J., 2020. Space weathering by simulated micrometeorite bombardment on natural olivine and pyroxene: a coordinated IR and TEM study. Earth Planet. Sci. Lett. 530, 115884. https://doi.org/10.1016/j.epsl.2019.115884.

Wenk, E., Schwander, H., Wenk, H.R., 1965. Labradorit von Surtsey (island). Acta Natur. Islandica II 5.

Winslow, R.M., Philpott, L., Paty, C.S., Lugaz, N., Schwadron, N.A., Johnson, C.L., Korth, H., 2017. Statistical study of ICME effects on Mercury's magnetospheric boundaries and northern cusp region from MESSENGER. J. Geophys. Res. Space Physics 122, 4960–4975. https://doi.org/10.1002/2016JA023548.

Wurz, P., Lammer, H., 2003. Monte-Carlo simulation of Mercury's exosphere. Icarus 164, 1–13 https://www.sciencedirect.com/science/article/pii/S0019103503001234{#}FIG 001. https://doi.org/10.1016/S0019-1035(03)00123-4.

Wurz, P., Whitby, J.A., Rohner, U., Martín-Fernández, J.A., Lammer, H., Kolb, C., 2010. Self-consistent modelling of Mercury's exosphere by sputtering, micro-meteorite impact and photon-stimulated desorption. Planet. Space Sci. 58, 1599–1616.

Yang, Y., Zhang, H., Wang, Z., Yuan, Y., Li, S., Hsu, W., Liu, C., 2017. Optical spectroscopic characterizations of laser irradiated olivine grains. Astron. Astrophys. 597, A50. https://doi.org/10.1051/0004-6361/201629327.

Young, C.L., Poston, M.J., Wray, J.J., Hand, K.P., Carlson, R.W., 2019. The mid-IR spectral effects of darkening agents and porosity on the silicate surface features of airless bodies. Icarus 321, 71–81. https://doi.org/10.1016/j.icarus.2018.10.032.

Zolotov, M.Y., Sprague, A.L., Hauck, S.A., Nittler, L.R., Solomon, S.C., Weider, S.Z., 2013. The redox state, FeO content, and origin of sulfur-rich magmas on Mercury. J. Geophys. Res. Planets 118, 138–146. https://doi.org/10.1029/2012JE004274.